High Resolution Portable Platform for pH sensing via Colorimetric Fluorescence of Carbon Dots

Gianluca Minervini[a,b,c], Annamaria Panniello[c], Daniel Quesada-González[a], Gabriel Maroli[a,e], Elisabetta Fanizza[c,d], Marinella Striccoli[c], Ruslan Álvarez-Diduk[a]*, Maria Lucia Curri[c,d]*, Arben Merkoçi[a,f]*

[a] Catalan Institute of Nanoscience and Nanotechnology (ICN2), CSIC and BIST, Campus UAB, Bellaterra, 08193 Barcelona, Spain

[b] Department of Electrical and Information Engineering, Polytechnic of Bari, via Orabona 4, 70126 Bari, Italy

[c] CNR-Institute for Physical and Chemical Processes (IPCF), via Orabona 4, 70126 Bari, Italy

[d] Chemistry Department, University of Bari "Aldo Moro", via Orabona 4, 70126 Bari, Italy

[e] Research Institute of Electrical Engineering (IIIE) "Alfredo Desages", National University of the South, CONICET- Argentina.

[f] Catalan Institution for Research and Advanced Studies (ICREA); Passeig de Lluís Companys, 23, Barcelona, 08010, Spain

* Corresponding Authors: Ruslan Álvarez-Diduk: ruslan.alvarez@icn2.cat; Maria Lucia Curri: marialucia.curri@uniba.it; Arben Merkoçi: arben.merkoci@icn2.cat.

Abstract

Portable sensing platforms based on nanoparticles are becoming increasingly significant across diverse fields, as they enable real-time measurements in various environments without complex lab protocols. Carbon dots (CDs), known for low toxicity and intense fluorescence, can exhibit pH-dependent optical emission, generally related to proton exchange-capable surface groups. In addition, CDs' hydrophilicity, biocompatibility, and stability make them advantageous for pH sensing and, despite limited application in portable sensing devices, their full potential can be realized with precise control of chemistry and optical properties. In this study, we fabricate a

30 portable nitrocellulose-based platform for pH sensing, expressly designed to take advantage of the

31 fluorescence properties of resorcinol-based CDs. First, responsivity of CDs fluorescence features

32 on pH is carefully spectroscopically characterized and linked to acid-base equilibria of

33 polyphenols (hydroxylated polyaromatic rings) present within the CDs carbonaceous structure.

34 Notably, this also offers a titrimetric method to estimate CD concentration. Next, nitrocellulose-

35 based wax-printed circular pads are functionalized with CDs and integrated with a smartphone-

36 based fluorescence colorimetric optical detection system. The developed portable device exhibits

37 a measurement resolution of ±0.2 pH units (in the range between 2.5 to 6.7) and of ±0.3 pH units

38 (in the 6.7 – 7.0 range), compatible with most practical pH measurement needs in biological, food

39 and drink, wastewater sample analysis and others. Moreover, although some portable pH sensing

40 devices are already widespread and commercially available, this platform is easy to use, it

41 necessitates only very small sample volumes and is potentially adaptable to various environments

42 and automated analysis processes that does not need prior-use calibrations.

44

45

1.   Introduction

47   In current real-world applications pH sensing is typically conducted using three-electrode

48 potentiometry (pH meters) or colorimetric pH test paper strips [1–4]. Specifically, potentiometric

49 pH meters offer a broad detectable pH range and very high resolution, while pH test strips provide

50 rapid pH testing, compatible with user-friendly procedures. However, in some practical scenarios,

51 these methods still suffer from limitations hindering their complete suitability. For instance, using

52 pH meters implies dealing with some drawbacks such as electrode vulnerability, the need for large

53   sample volumes, necessity of frequent calibration and trained operators. On the other hand, in most

54   usual cases, commercial pH test strips are characterized by measurement resolutions not higher

55   than ca. ±0.5 pH units [5,6]. Furthermore, certain colorimetric tests require visual interpretation of

56   the results, which can be disadvantageous due to the potential for personal color biases in

57   determining pH values [7,8].

58   In response to these colorimetric detection limitations, recent efforts have aimed at

59   advancing such classical pH testing methods. This has led to the fabrication of sophisticated pH

60   sensor devices with optical detection, as emphasized by several works reported in the scientific

61   literature [8–22] and in recently patented inventions [23–25]. Generally, these advanced devices

62   consist of an active pH sensing material embedded or deposited onto a substrate matrix (often

63   paper- or polymer-based). The active material responds to pH variations with detectable alterations

64   of its optical properties. In particular, the revelation of such optical property variations, either via

65   smartphone- or desktop-scanner-based detection then enables improvements on measurement

66   objectivity and accuracy [8,12,14–16,18–22]. Nevertheless, such innovative pH sensing platforms

67   often face technical limitations, including a narrow dynamic range (sometimes limited to few pH

68   units), long response times, the need for large sample volumes , and accuracy in pH determination

69   not significantly higher than that of commercial pH strips [9–11,13,16,17,19–22]. Moreover, other

70   reported methods require multi-step fabrication procedures (e.g. based on high-resolution laser

71   patterning of the substrate, or ink-jet printing using separate custom-made inks) that must be

72   devised with extensive care to ensure the proper working of the final sensing device [8,12–15,17–

73   22]. Thus, there is generally still demand for development of robust and high-performing

74   colorimetric pH sensors.

75   CDs, zero-dimensional carbonaceous nanoparticles characterized by visible-light

3

76 fluorescence, have attracted attention as pH sensing materials since early stages of their discovery

77 [26–28]. These nanoparticles typically have a size between 1 and 10 nm and they are chemically

78 composed of non-toxic light elements (C, O, H, and eventually N, S, P, B, …) [29–33]. Many CDs

79 synthesized via carbonization of water-soluble molecules naturally exhibit fluorescence properties

80 that respond to pH changes [27,28]. This responsiveness is typically ascribed to the presence of

81 acid/base active surface chemical groups, such as –COOH, –NH$_2$, –OH, etc. [26]. Therefore, CDs

82 have been widely reported as pH-sensitive materials in aqueous dispersions [26–28]. More

83 specifically, depending on their spectroscopic features, single-band emitting CDs have been

84 employed for pH sensing based on fluorescence quenching, while multiple band emitting CDs

85 have been often proposed for ratiometric fluorescence sensing [34–38].

86 Often, CDs are used directly in solution-based analyses, providing highly accurate pH

87 measurements [26,39,40]. Nevertheless, these techniques necessitate benchtop instrumentation

88 and experienced personnel. Meanwhile, the incorporation of these nanoparticles into portable

89 platforms has been reported in few examples. Wang et al. [41] prepared pH test strips embedding

90 orange-emitting CDs that exhibited naked-eye observable changes in fluorescence intensity across

91 the pH range of 1–14 when examined under UV light. Zhang et al. [42] ink-jet printed pieces of

92 filter paper with tricolor emitting CDs to obtain pH test strips that could successfully measure pH

93 in a broad range by visual inspection of color changes. Huo et al. [43], reported a polymer based

94 pH sensor based on CDs as sensing materials that, after soaking for 5 s in a buffer solution, allowed

95 quantitative pH assessment after recording the fluorescence with a spectrofluorometer and

96 employing fluorescence or colorimetry to quantify the sensing signal. Thus, in spite of the large

97 number of papers reporting pH sensing with CDs in solution, the application of these nanoparticles

98 in portable platforms using advanced optical signal registration remains limited and needs to be

99   further explored.

100   With this motivation, in this work, we develop a portable pH sensing platform based on

101   colorimetric fluorescence CD detection. Dual emissive CDs are synthesized by polycondensation

102   of resorcinol and containing acid-base optically responsive hydroxylated polyaromatic rings [44].

103   The mechanism enabling the pH sensing relies entirely on the fluorescence properties of the CDs.

104   First, the fluorescence pH responsivity of the CDs is carefully examined and correlated to acid-

105   base equilibria at the molecular level. Then, the fluorescent nanoparticles are used to functionalize

106   wax-printed pads on a nitrocellulose substrate. Fluorescence changes with pH are assessed using

107   colorimetric image analysis, which allows achieving high-resolution pH measurement, reaching

108   ±0.2 pH units in the range from $2.5 - 6.7$ pH range and ±0.3 pH units in the $6.7 - 7.0$ range.

109   Overall, the approach presented herein is compatible with a broad variety of samples and working

110   conditions and hence can have applicative relevance for pH sensing in several areas.

111   **2.   Materials and Methods**

112   2.1 Chemicals

113   Resorcinol ($\geq$99%, Sigma Aldrich), ethylene glycol (EG, $\geq$ 99%, Sigma Aldrich), sodium

114   hydroxide (NaOH, $\geq$97%, Sigma Aldrich), hydrochloric acid (HCl, 37%, Sigma Aldrich),

115   disodium hydrogen phosphate (Na_2HPO_4, 98-100.5%, Sigma Aldrich), monosodium dihydrogen

116   phosphate (NaH_2PO_4, $\geq$99.0%, Sigma Aldrich), citric acid (99%, Sigma Aldrich), L-ascorbic acid

117   (AA, 99%, Sigma Aldrich), sodium carbonate (Na_2CO_3, $\geq$99.5%, Sigma Aldrich), sodium

118   bicarbonate ($NaHCO_3$, $\geq$99.7%, Sigma Aldrich). McIlvaine (citrate-phosphate) buffer solutions at

119   pH ranging from 8 to 2.2 were obtained mixing stock solutions of 0.1 M citric acid and 0.2 M

120   Na_2PO_4 in different volume ratios up to reaching a final volume of 5 mL.[45] Carbonate-

5

121 Bicarbonate buffer at pH 10 was analogously obtained by mixing adequate volumes of 0.1 M stock

122 solutions of Na_2CO_3 and $NaHCO_3$. All aqueous solutions were prepared using MilliQ water.

123 ## 2.2 Preparation of CDs

124   CDs were synthesized following a procedure previously reported in [44]. In details, a

125 solution of resorcinol (1.5 g) in EG (3 mL) was added to 12 mL of EG previously heated in a round

126 bottom flask that was kept open through all the duration of the reaction. Soon after resorcinol

127 solution injection, 500 μL of a 2 M NaOH aqueous solution were quickly added, serving as a

128 catalyst for resorcinol carbonization. The reaction temperature in the round bottom flask was

129 monitored and kept constant *via* a temperature controller connected to a heating mantle by a

130 thermocouple placed inside the flask. After synthesis, the obtained CDs were purified by a series

131 of four successive centrifugation steps, using a very diluted ($\sim10^{-4}$ M) HCl aqueous solution to

132 recollect and precipitate the nanoparticles. More specifically, after each centrifugation step at

133 9000 rpm for 30 min, the supernatant was removed and discarded, while the purified precipitate

134 was redispersed adding $\sim10^{-4}$ M HCl solution. Finally, after four centrifugation cycles, the dark

135 precipitate was dried under vacuum. The as-obtained purified CDs were finally dispersed in

136 aqueous buffer solutions for further uses.

137 ## 2.3 Spectroscopic analysis of CD optical properties

138   UV-Vis absorption spectra were acquired with a Cary 5000 spectrophotometer (Agilent

139 Technologies, Inc., Santa Clara, CA, USA). Photoluminescence (PL) spectra were measured with

140 a Fluorolog 3 spectrofluorometer (HORIBA Jobin-Yvon GmbH, Bensheim, Germany) equipped

141 with a 450 W Xe lamp as the excitation source and with double-grating excitation and emission

142 monochromators. All measurements were performed on dispersions of CDs in aqueous buffer

143 solutions, in a quartz cuvette (Hellma Analytics, Milan, Italy) with a 1 cm optical path. To avoid

144 photon re-absorption in these measurements, all solutions were diluted so that the absorbance

145 registered at the maximum of the lower energy absorption band was less than 0.1.

146 2.4 pH-sensitivity of CDs experiments in solution

147 Purified CD powders were dispersed in a phosphate buffer solution (0.1 M, pH = 7) that

148 was previously prepared by mixing suitable concentrations of Na_2HPO_4 and NaH_2PO_4.

149 Subsequently, 1 mL of such CD dispersion (having a concentration of 5 µg/mL) was subjected to

150 the incremental addition of a 1 M HCl aqueous solution (HCl_{aq}). Specifically, at each step of HCl

151 addition, 5 µL of HCl_{aq} were added and UV-Vis absorption and PL (λ_{exc} = 350 nm, λ_{exc} = 485 nm)

152 spectra were recorded. The experimental procedure was concluded upon reaching a total added

153 volume of 105 µL, as no further discernible spectroscopic changes were observed. To account for

154 the dilution introduced upon addition of the HCl_{aq}, the as-recorded spectra were multiplied by a

155 factor:

156 $$D = \frac{V_{in} + V_{add}}{V_{in}} \tag{1}$$

157 where V_{in} is the initial volume of the CD dispersion and V_{add} is the added volume of HCl.

158

159 2.5 Fabrication of CD-based nitrocellulose pads and smartphone-based fluorescence

160 detection

161 A nitrocellulose membrane strip (Unisart® CN95, Sartorius) was patterned to create

162 circular nitrocellulose pads (CNPs) with a diameter of 2.5 mm spaced by a 1.5 mm distance. The

163 pattern was created by printing a black hydrophobic wax using a Xerox ColorQube 8580 solid ink

164 printer. After printing, the nitrocellulose strip was kept on a hot plate at 90 °C for 30 s to allow

165 diffusion of the hydrophobic wax across the entire thickness of the nitrocellulose, thus creating a

166 complete lateral confinement of the circular pad.

167   Then, the CNPs were functionalized by drop-casting 2 µL of a pristine aqueous dispersion

168   of CDs, followed by drying on a hot plate at 50 °C for 15-20 min, until complete water evaporation.

169   Thus, functionalized circular nitrocellulose pads (F-CNPs) were obtained. To construct the

170   calibration curves, the F-CNPs were drop-casted with 2 µL of McIlvaine buffer solutions at

171   different pH values.

172   The resulting modifications of CD fluorescence were then analyzed with a Microscopy

173   Cube Assembly (TLV-U-MF2, THORLABS[©]), equipped with an excitation filter (MF390-18,

174   390 ± 9 nm), a dichroic filter (MD416 425 – 575 nm) and optional emission filters (MF460-60,

175   460 ± 30 nm, referred to as "blue emission filter" or MF530-43, 530 ± 20 nm, referred to as

176   "green emission filter"). The employed setup allowed irradiating and analyzing four F-CNPs in

177   each single acquisition. Each pool of four pads contained one pad drop-casted with a pH 8

178   McIlvaine buffer, that was used as internal reference in the case of single-channel intensity

179   analyses.

180   The fluorescence was then detected recording digital pictures with a smartphone camera

181   (Realme GT NEO 3T) in manual mode, autofocus, ISO at 100 and adjusting the shutter speed in

182   order to optimize the exposure conditions.

183

184   **3. Results and discussion**

185

186   3.1 CDs preparation, characterization and PL mechanisms underlying pH

187   responsivity

188   The preparation of CDs employed for the portable platform relies on a method reported in

189   [44] and is schematized in Fig. 1a. The synthetic approach involves thermal polycondensation of

190 resorcinol in ethylene glycol solvent and basic-catalyzed environment. This leads to the formation

191 of CDs containing PPs, i.e. hydroxylated polyaromatic molecules, deriving from resorcinol
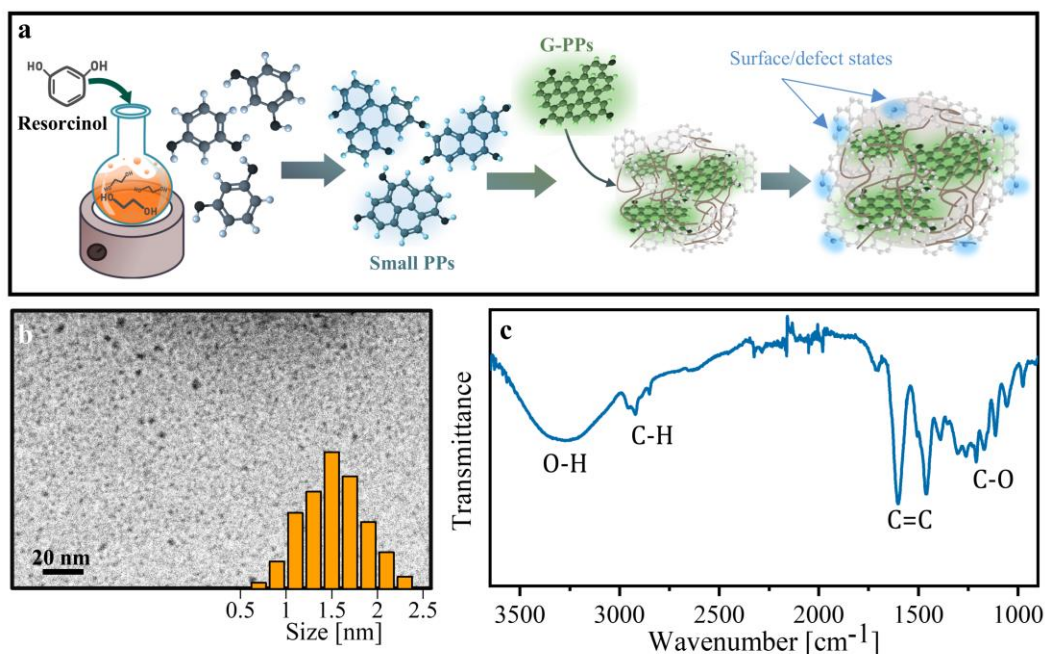
192 polycondensations.

193

194 **Fig. 1.** (a) Scheme of synthetic preparation of CDs and of formation of fluorescent PPs in the

195 nanoparticles during the reaction. (b) TEM micrograph and size distribution histogram (inset) and

196 (c) FT-IR spectrum of the CDs.

197

198   The CDs are observable in TEM micrographs as spheroidal dots having a mean size of

199 1.5 ± 0.3 nm (Fig. 2b). The FT-IR spectrum of CDs displays a broad band ascribed to O–H

200 stretching (at $3320 – 3600$ cm^{-1}), some weak peaks in the $2800 – 3000$ cm^{-1} interval due to C–H

201 stretching, some signals due to C=C stretching (at $1650 – 1750$ cm^{-1}) and peaks in the region

202 $1000 – 1300$ cm^{-1} due to C–O stretching. Such FT-IR analysis highlights that the CD surface

203 contains hydroxyl groups. Moreover, both aromatic and aliphatic carbon structures are identified

204 in the CDs. Additionally, the broad O–H stretching band indicates the formation of hydrogen

205 bonds between the alcohol functionalities. This aligns well with model in [44]. that describes CDs

206 as consisting of PPs incorporated in a carbogenic nanoparticle matrix, interconnected by EG-

207 aliphatic structures and stabilized via hydrogen bonds.

208   The sensing mechanism in the portable platform derives from the response of the CD,

209 particularly to the response of this fluorescence to pH, and needs to be further assessed. UV-Vis

210 absorption and (PL) spectra of resorcinol-derived CDs are reported in Fig. S1. The CD absorption

211 spectrum exhibits a narrow band at around 500 nm and an extended absorption at $\lambda < 400$ nm. The

212 emission spectrum consists of a blue and a green PL band. As recently demonstrated in [44] and

213 resumed in Table S1 these are respectively ascribed to emission by surface or defect states and to

214 the molecular emission of green emitting PPs (G-PPs).

215   To specifically test in detail the reversible responsivity of CD fluorescence to pH changes,

216 we carried out an experiment in which CDs in solution were progressively added with a very small

217 number of HCl moles, while modifications of spectroscopic absorption and emission features were

218 monitored after each addition. For this experiment, first, CDs were dispersed in a phosphate buffer

219 at pH 7 and then mixed with 5 μL of 1 M solutions of HCl in successive steps (see Sec. 2.4 for

220 further details). Spectroscopic changes observed in UV-Vis absorption and PL spectra

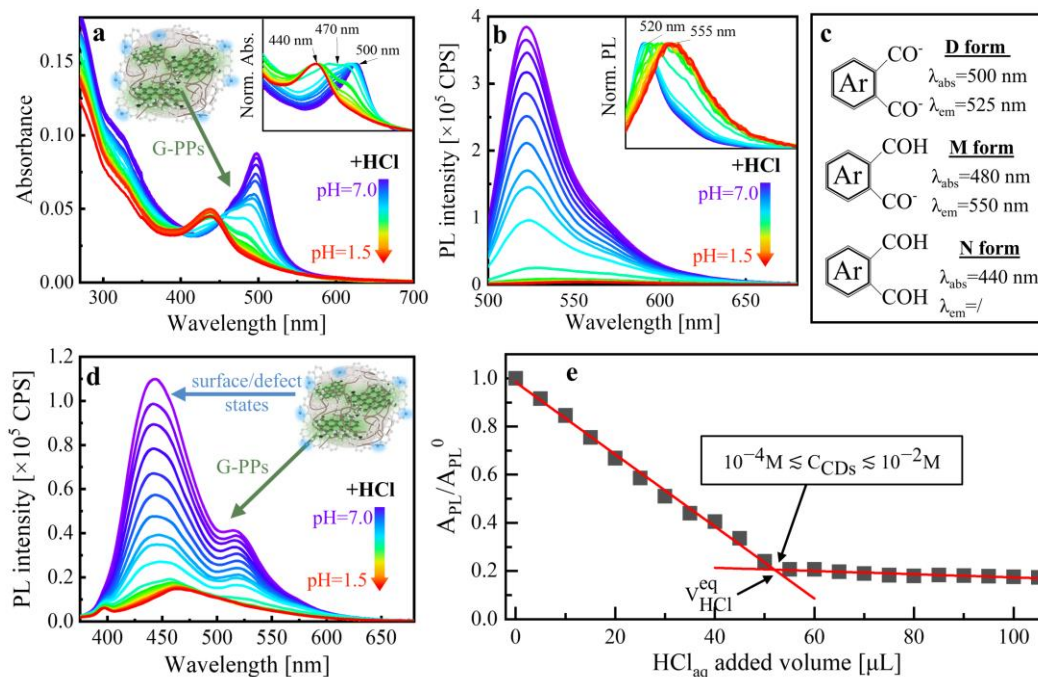221 ($\lambda_{exc} = 485$ nm) after each HCl addition are reported in Fig. 2a-b.

Fig. 2. (a) UV-Vis absorption and (b) PL ($\lambda_{exc} = 485$ nm) spectra of a CD dispersion at increasing HCl concentration, with top-right insets showing normalized spectra and peak positions; (c) scheme of the dianion (D), monoanion (M) and neutral (N) forms of the green-emitting polyphenols (G-PPs), including their absorption and emission peak positions; (d) PL spectra ($\lambda_{exc} = 350$ nm) of CDs at increasing HCl concentration. Insets of (a) and (d): scheme of the CDs designating with blue and green band assignments, initial and final pH; (e) fluorescence titration curve reporting the ratio between PL spectrum areas $\lambda_{exc} = 350$ nm (A_{PL}) and that of the pristine solution spectrum (A_{PL}^0) as a function of the volume of added titrant.

Upon the incremental HCl addition, the absorption band at 500 nm of the pristine CDs dispersion exhibits a gradual dampening and a large blue shift (Fig. 2a). Specifically, Fig. 2a inset clearly shows that the pristine absorption band undergoes a transition to a band at 470 nm and

11

235 finally to a band peaked at 440 nm. In parallel, a substantial quenching of the green PL peak

236 (Fig. 2b), with a progressive red shift of the pristine band (Fig. 2b inset), is noted.

237   Such spectroscopic variations can be explained considering the possible proton-

238 exchanging equilibria of PPs in dependence of pH. In fact, it is known that hydroxylated

239 polyaromatic molecules can have pKa in physiological pH ranges [46–48] and that the surface of

240 these CDs is negatively charged due to the hydroxyl groups' deprotonation [44]. Therefore, to

241 rationalize the observed spectroscopic changes with HCl addition, we can safely consider that in

242 the pristine solution (at pH 7) the G-PPs have some –CO^- groups that can quantitatively react with

243 H^+. Upon HCl addition, these groups are progressively protonated to –COH, leading to the

244 observed spectroscopic modifications. Conversely, after reaching a pH of 1.5, the absence of

245 additional changes upon further HCl addition suggests that, under these pH conditions, the

246 polyaromatic fluorophores lack –CO^- groups that can quantitatively react with H^+. Thus, the

247 spectral band shifts and modifications observed both in absorption and PL can be collectively

248 explained considering three distinct acid/base conjugated forms for the G-PPs (Fig. 2c), namely:

249 (i) a dianion (D) form responsible for the pristine absorption at 500 nm and emission at 520 nm,

250 (ii) a monoanion (M) form absorbing at around 470 nm and weakly emitting at 555 nm and (iii) a

251 neutral (N) form, that has the absorption band peaked at 440 nm and no emission within the

252 investigated spectral range.

253   To demonstrate the reversibility of the acid-base reactions between the D, M and N forms,

254 the acidified dispersion of CDs (pH 1.5) was progressively added with 5 μL of a 1 M NaOH

255 aqueous solution. The resulting spectroscopic data collected after each NaOH addition are reported

256 in Fig. S2a-b. It can be observed that NaOH addition leads to a fluorescence restoration retracing

257 the spectroscopic changes of the HCl quenching. However, a slight loss of fluorescence intensity

258   is observed, as demonstrated by the difference between the restored PL intensity at pH 7 and the

259   original one, that is ascribed to irreversible phenomena occurring during such experiments, such

260   as nanoparticle aggregation or irreversible chemical modifications of the emitting units within the

261   CDs, hindering the complete reestablishment of the original fluorescence intensity [44].

262   The overall PL spectrum consists of a blue and a green PL band, as can be revealed exciting

263   the CDs in the UV range (Fig. S1). Thus, to provide a comprehensive overview of pH sensitivity

264   of both CD emission bands, we examined the variations in the PL spectra obtained after HCl and

265   NaOH additions exciting at 350 nm (Fig. 2d, Fig. S2c).

266   With the progressive increase of added HCl, both blue and green PL bands exhibit a gradual

267   decrease in the intensity. On the other hand, addition of NaOH to the quenched solution leads to

268   restoring both bands, with a fluorescence loss (Fig. S2c). Remarkably, upon quenching and

269   restoration, the relative intensities of the blue and green PL bands undergo variations. This can be

270   easily shown for instance, by plotting the ratio of the intensities of the two bands recorded at their

271   maxima (i.e. 445 nm and 520 nm), as a function of volume of added titrants (namely HCl and

272   NaOH), as shown in Fig. S3. For the quenching experiment, the ratio between blue and green PL

273   band intensities shows two uniform progressive decrease trends in the range of added titrant (i.e.

274   HCl) volume from 0 to 45 μL and from 60 to 105 μL, interspaced by a small increasing trend from

275   45 to 60 μL. On the other hand, in the restoration experiment the ratio undergoes an increase upon

276   addition of the first 10 μL of titrant (i.e. NaOH), then it remains constant up to a volume of 70 μL,

277   after which it progressively increases up to reach around the value of the pristine solution at the

278   added NaOH volume of 105 μL. The results collectively show that the individual blue and green

279   PL bands not only can be reversibly quenched and restored, but also their ratio undergoes some

280   reversible variations as an effect of quantitative reactions with HCl and NaOH. Notably, this

281 change of blue-to-green relative intensities constitutes the foundation for the application of the

282 fluorescence colorimetry approach, as described in the following.

283 From an applicative perspective, it is also noteworthy that, despite the high sensitivity of

284 the blue and green PL bands to pH, the PL of the nanoparticles remains unaffected by other

285 possible interferents, such as metal cations or biological vitamins, even at high concentrations

286 (≥ 50 mM). The potential interference of these species in pH analysis was suitably evaluated, and

287 the results are provided in the SI (see Fig. S4 – S6).

288 Furthermore, the discovery that also the blue PL band alone exhibits a reversible pH

289 sensitivity, indicates that, akin the G-PPs, surface and/or defect groups responsible for this PL

290 band undergo reversible chemical protonation reactions. In particular, considering that the

291 chemical composition of CDs is characterized by variably protonated hydroxyl functionalities, [44]

292 it may be recognized that these groups are reversibly protonable –CO⁻ groups.

293 Thus, considered collectively, the results of the previous experiments evidence that the titrant (HCl)

294 quantitatively reacts with both (i) G-PPs and (ii) –CO⁻ groups of different PPs that can undergo

295 protonation reactions. This may also spontaneously inspire to consider the quenching experiment

296 (Fig. 2d) as a fluorometric titration of such species featuring reversibly protonable –CO⁻ groups

297 (Fig. 2e). In particular, with appropriate considerations on the reaction stoichiometry and on the

298 density of emitting units present in each nanoparticle, we can correlate the volume of titrant at the

299 equivalence point (V_{HCl}^{eq}) to the molar concentration of nanoparticles in the dispersion (C_{CDs}), with

300 the equation:

301 $$C_{CDs} = \frac{C_{HCl} V_{HCl}^{eq}}{s_m d_{EM} V_{in}} \tag{2}$$

302 where C_{HCl} is the concentration of the titrant stock solution, V_{in} is the initial volume of the pristine

303 dispersion of CDs, s_m is the average stoichiometry of reactions of H^+ and d_{EM} is the density of

304 emitting units per CD. Complete details regarding the derivation of Eq. (2) are provided in the SI.

305   It is interesting to note that Eq. (2) may allow estimating the concentration of CDs in a

306 dispersion by means of a titration method, i.e. measuring the volume of titrant at the equivalence

307 point. However, it is evident that a precise C_{CDs} obtainment needs that s_m and d_{EM} are known. In

308 turn, accurate assessment of these quantities demands additional expressly focused experimental

309 procedures, and/or a very extensive theoretical modelling of the carbonaceous nanoparticles.

310 Therefore, the correct calculation or experimental determination of s_m and d_{EM} is not the scope of

311 this work. However, the orders of magnitudes of these quantities can be reasonably individuated.

312 In the SI, a detailed discussion is provided in which the approximate orders of magnitude for the

313 upper and lower bounds of s_m and d_{EM} are rationally examined. By setting such rough bounds for

314 s_m and d_{EM} and substituting the measured V_{HCl}^{eq} in Eq. (2), a reasonable range of order of

315 magnitude for C_{CDs} can be evaluated, which is between 10^{-4}–10^{-2} M. In general, it is worth

316 remarking that a more precise estimation of s_m and d_{EM} would result in a better estimate of the CD

317 concentration. This could represent a significant stride towards establishing reliable procedures for

318 determining the amount of CDs in a solution, a critical advancement for broadening the practical

319 applications of CDs across various fields.[49]

320

321 3.2 Design of nitrocellulose-based platform and its sensing mechanism

322   The nitrocellulose-based platform exploits the intriguing fluorescence response of CDs due

323 to reversible protonation of G-PPs and hydroxyl surface groups. The preparation of the

324 nitrocellulose substrate consisted in a simple fabrication of CNPs, by printing a hydrophobic wax

325 (the complete experimental procedure is described in the Experimental Section). After their

326 preparation, the CNPs were functionalized by drop-casting an aqueous CD dispersion, followed

327 by water evaporation under soft heating. CDs were thus immobilized on the surface of the CNPs

328 yielding F-CNPs.

329   The principle underlying pH sensing in the platform can be summarized as follows: upon

330 drop-casting a calibration solution (McIlvaine buffer, composed by a citrate-phosphate acqueous

331 solution) onto the F-CNPs, a fraction of the CDs in the F-CNPs are solubilized in the aqueous

332 phase of the deposited drop. Once in the aqueous phase, interaction of CDs with H^+ in the buffer

333 solution leads to alterations of the CD fluorescence that are analyzed by a smartphone-based

334 detection system. In particular, the optical revelation device is equipped with mirrors and filters

335 suitable for discrimination of the blue and green fluorescence contributes deriving from the CDs

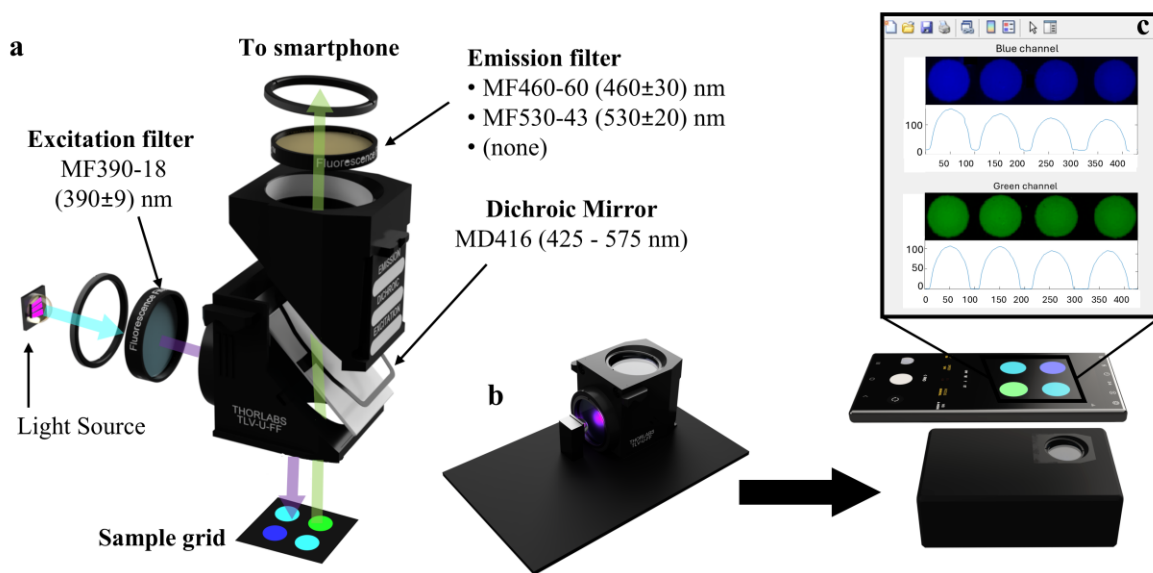336 (Fig. 3) (for further technical specifications see Experimental Section).

337

338 **Fig. 3.** (a) scheme of the fluorescence detection system equipped with dichroic mirror and optical

339 excitation and emission filters. Optical emission filters with bandwidths of (460 ± 30) and

340 (530 ± 20) nm are denoted in the text as "blue" and "green" emission filters respectively; (b)

341 overview of the portable fluorescence detection device operating with the smartphone; (c)

342 software-based analysis of the fluorescence from CDs in the functionalized circular nitrocellulose

343 pads (F-CNPs). More details on fluorescence digital picture analysis are reported in the following

344 section regarding the calibration of nitrocellulose pad fluorescence for pH sensing.

345

346 ## 3.3 Calibration of nitrocellulose pad fluorescence for pH sensing.

347 Within the pH sensing strategy of the developed platform, the fluorescence signal needs to

348 be maximized adjusting the concentration and protonation state of the pristine CD dispersion

349 employed to obtain the F-CNPs. First, the concentration of CDs deposited in the F-CNPs is a

350 pivotal parameter to calibrate as it will influence the overall fluorescence intensity. CD

351 concentration in the initial dispersion was calibrated by depositing pristine CD dispersions at

352 increasing nanoparticle concentration on CNPs. The PL was then revealed using the smartphone-

353 based apparatus (Fig. 3). Smartphone recorded digital pictures were acquired at different exposure

354 times, obtained by modulating the shutter speed in the range 0.2 – 0.5 s and employing blue and

355 green emission optical filters (Fig. 4). Following acquisition, the digital pictures were processed

356 to separate their three-color channels: Red (R), Green (G) and Blue (B). Details of such image

357 analysis procedure are described in the SI (see Fig. S7). Subsequently, as shown in Fig. 4c-d, the

358 intensity of each channel is analyzed separately. Then, the fluorescence is evaluated quantitatively

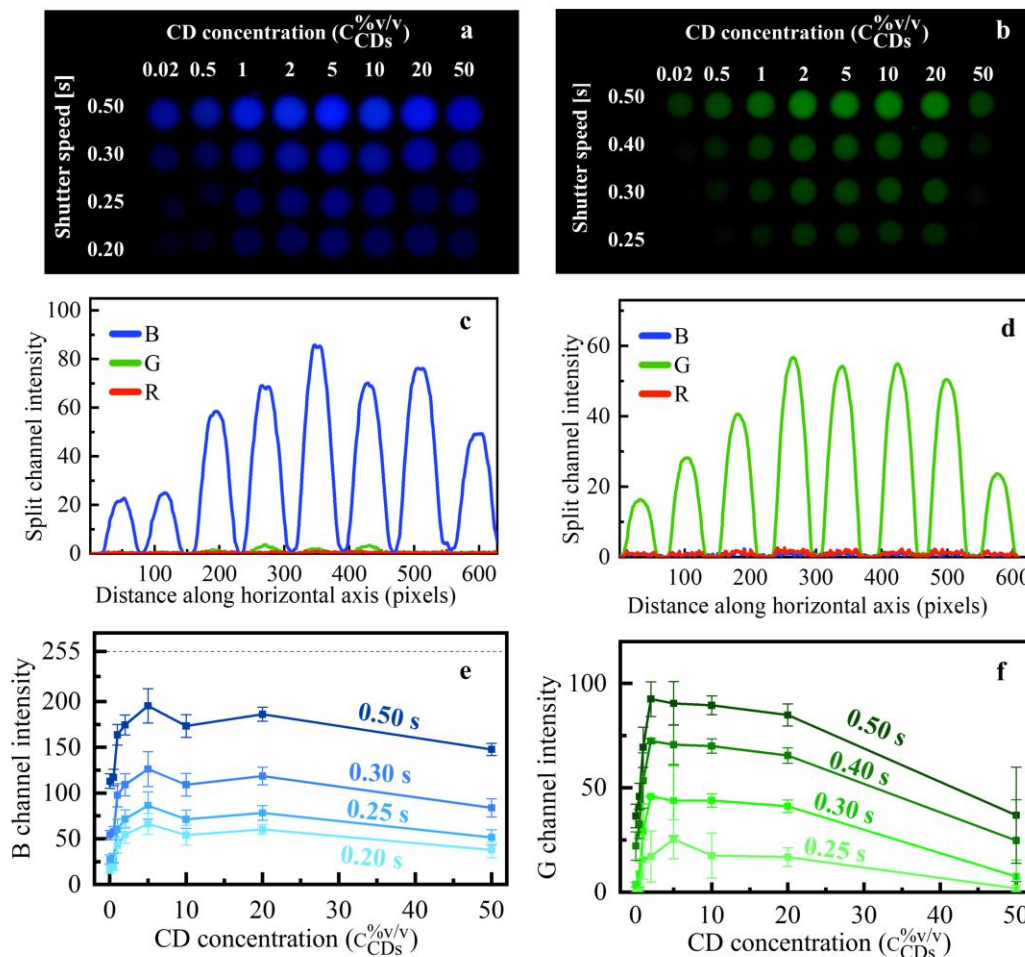359 from the intensities of B or G channels, as shown in Fig. 4e-f.

360

Fig. 4. (a), (b) smartphone recorded digital pictures of the F-CNPs at different shutter speeds and CD concentrations ($C_{CDs}^{\%v/v}$); (c), (d) plots of B, G and R channels as a function of the distance along the horizontal axis of the picture (F-CNPs spots at the third row of (a), (b) were selected as representative, corresponding to shutter speed of 0.25 and 0.30 s for the B and G channels respectively), and (e), (f) resulting B and G channel intensities of F-CNPs drop-cast with CD dispersions at $C_{CDs}^{\%v/v}$ from 0.02 to 50%$_{v/v}$. Pictures and B, G channel intensities have been acquired using (a), (c), (e) blue emission filter and shutter speed in the range of 0.20 – 0.50 s and (b), (d), (f) green emission filter and shutter speed in the range of 0.25 – 0.50 s. The upper scale limit of

369   the grayscale range (0 – 255) is highlighted in (e) as a guide for the eye. The error bars are standard

370   deviations calculated from three experiment replicates.

371

372   From Fig. 4c it appears evident that the use of the blue emission filter leads to a

373   fluorescence signal exclusively in the B channel and only very low residual signal intensity is

374   noted in the G channel, while the R channel registers only noise. Vice versa, upon the application

375   of the green emission filter (Fig. 4d), only the G channel reveals a discernible signal, while the B

376   and R channels exhibit noise exclusively. This confirms that the blue and green emission filters

377   allow independent analysis of the spectroscopic blue and green PL bands of the CDs (Fig. 2b,

378   Fig. 2d, Fig. S1).

379   The signal intensities of B and G channels obtained after quantitative digital image analysis

380   (Fig. 4e-f) allow assessing the alterations of fluorescence intensity of blue and green PL bands due

381   to changes in nanoparticle concentration and shutter speed. For both B and G channels, the

382   intensity increases linearly with the CD concentration up to 2 %; then, a saturation range is

383   observed in the 2 – 20 % interval, as the points of recorded intensities in this range are invariant

384   within the experimental error. Subsequently, a decrease of fluorescence intensity is obtained upon

385   further CD concentration increase beyond 20% up to 50 %.

386   Such fluorescence self-quenching phenomenon at increasing concentration occurs in

387   numerous fluorophores, [50–52] including CDs [53–57] and it is often ascribed to the re-

388   absorption of emitted photons due to overlapping of absorption and fluorescence bands, or to

389   transfer processes. Remarkably, the results in Fig. 4e-f highlight that the dampening due to photon

390   re-absorption is more pronounced for the G intensity than for B intensity. This tightly agrees with

391   the spectroscopic properties of CDs (Fig. S1) and can be explained considering that the green

392 emission band has a very small Stokes shift. This remarks how changes in CD spectroscopic

393 features observed in cuvette and using a benchtop spectrofluorometer (see Sec. 2.3) are retained

394 in the B and G channels after deposition on CNPs and image analysis. It also worth to note that

395 the trends of B and G channel intensity with $C_{CDs}^{\%v/v}$ result independent from the shutter speed, that

396 just alters the intensity of the recorded PL but not the trend of the intensity with $C_{CDs}^{\%v/v}$. This points

397 out that the exposure time can be flexibly adjusted within the interval from 0.2 to 0.5 s, to optimize

398 the signal-to-noise ratio in the resulting pictures.

399 Besides nanoparticle concentration, the state of protonation of –CO$^-$ groups of CDs is

400 another crucial parameter to optimize. In fact, protonation of hydroxyl groups determines

401 alterations of the overall PL intensity emitted by the CDs (Fig. 2, Fig. S2), and also of the ratio

402 between blue and green PL bands (Fig. S3). Within the preparative approach, the protonation state

403 of CDs can be modified by altering the pH of the pristine dispersion employed for the

404 functionalization of CNPs. Thus, we tested different combinations of $C_{CDs}^{\%v/v}$ and pH values of

405 pristine CD dispersion, aimed at identifying the appropriate combination of parameters able to

406 maximize the responsivity to pH.

407 The detailed procedure of simultaneous pH and $C_{CDs}^{\%v/v}$ optimization of the pristine CD

408 dispersion is provided in the SI (Table S2-S3, Fig. S8 – S9). More specifically, we tested $C_{CDs}^{\%v/v}$ in

409 the range of 5 – 20 %, based on the finding that this saturation range allows nanoparticle

410 concentration adjusting without significant effects on fluorescence intensity (Fig. 4e-f).

411 Furthermore, we tested pristine solution pH in the range of 7 – 10, based on the observation that

412 the overall PL of the CDs is maximum at pH > 7, as indicated in Fig. S8a, where the samples at

413 fixed $C_{CDs}^{\%v/v}$ show brighter spotlights at higher pH values. For each examined case of F-CNP, a

414 calibration curve was constructed, thus allowing association of the parameters for CNP

415   functionalization with the sensing performance. These calibration curves were obtained by drop-

416   casting F-CNPs with McIlvaine buffer solutions in the pH range between 2.2 and 7 (Fig. S8c). The

417   procedure aimed at finding concentration and pH values of the CD pristine dispersion leading to

418   the best balance between wide pH dynamic range, high resolution in pH measurements, high

419   fluorescence intensity (leading to high signal-to-noise ratio in the acquired images) and low

420   spurious background signals. On the other hand, picture acquisition parameters, such as the shutter

421   speed, play a minor role in the optimization of experimental parameters, as they led only to slight

422   alterations in the normalized B channels (Fig. S10). Based on these quantitative assessments, the

423   dispersion having $C_{CDs}^{\%v/v}$ of 10 % and pH 8 was selected as the most favorable to functionalize

424   CNPs for further pH sensing experiments.

425   3.4 pH sensing with F-CNPs: the fluorescence colorimetry approach

426   As demonstrated in Fig. 4 and Fig. S7, fluorescence quantification from the digital pictures

427   can be achieved using optical emission filters to measure the intensity of either the B or the G

428   channel, resulting in a single-channel fluorescence detection strategy. Notably, when acquiring

429   digital pictures without emission filters (Fig. S8a-b), both the blue and green fluorescence bands

430   are revealed simultaneously, enabling an increase in the amount of information recorded in a single

431   acquisition. However, utilizing the sensing information from both channels simultaneously

432   requires an image analysis strategy that cannot be only based on examining the intensity of

433   individual B or G channels. To address this issue, the fluorescence recorded in the digital pictures

434   is analyzed in terms of colorimetric coordinates. Fig. 5 shows the fluorescence colorimetric

435   strategy used to sense pH with F-CNPs previously optimized (Fig. 4e-f, Fig. S8c, Table S2-S3).

436   The digital images in Fig. 5a depict the color of CDs fluorescence light in the absence of

437   emission filters. Thus, the F-CNPs show a blue-green color, attributable to the combined presence

438 of the blue and green PL bands in the recorded light (Fig. 2d, Fig. 4). Moreover, a progressive

439 shading from greener to bluer may be macroscopically inferred as the pH of the buffer calibration

440 solution increases from 2.2 to 8. Although this shift can be subtle making its discernment

441 challenging with the naked eye, it aligns with the spectroscopic trend showing an increase in the

442 ratio between the intensity of the blue and green PL bands as pH increases (Fig. S3). To provide a

443 more precise and objective quantification of this trend, a digital analysis of the fluorescence color

444 was performed. Fig. 5b outlines the process for deriving colorimetric coordinates from the

445 captured images. Similar to the method used to quantify the intensity of B and G channels reported

446 in the SI (see Fig. S7), the digital images were analyzed to generate a data matrix.
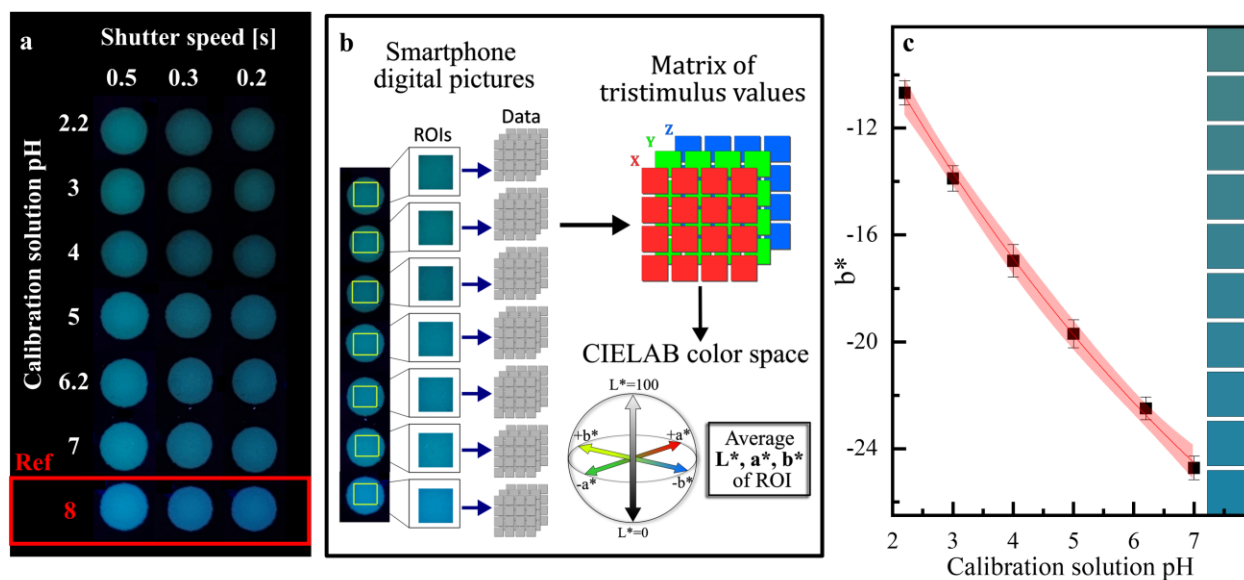

447

448 **Fig. 5.** (a) Smartphone recorded pictures obtained without emission filters at shutter speeds of 0.5,

449 0.3 and 0.2 s for F-CNPs functionalized with CD dispersion ML0810 (with optimized $C_{CDs}^{\%v/v} =$

450 10% and pH 8, see SI) and drop-casted with buffer calibration solutions at pH of 8, 7, 6.2, 5, 4, 3,

451 2.2; (b) schematic description of the image analysis procedure used to obtain the CIELAB

452 coordinates (L^*, a^* and b^*) from each F-CNP; (c) b^* coordinate of F-CNPs (shutter speed 0.5 s) as

453 a function of calibration solution pH (black squares), fitted using Equation (2) (red line). The red

22

454 shaded area represents the 95% confidence interval, the error bars are standard deviations obtained

455 from three replicates of the same experiment, the color scale legend on the right shows the

456 perceptual colors corresponding to b* varying in the range of y-axis coordinates for fixed $L^* = 50$

457 and a* = -20 (approximate average values of L^* and a^* obtained from the image analyses for shutter

458 speed of 0.5 s)

459

460   This matrix contains the intensity of the R, G and B channels for each pixel in the region

461 of interest (ROI). The R, G and B intensities were subsequently converted into X, Y and Z

462 tristimulus values using the sRGB color space which is the native color space of the pictures. The

463 standard illuminant assumed was D65, in line with CIE recommendations [58]. Finally, a

464 transformation was performed to obtain CIELAB 1976 color space coordinates [59], which were

465 averaged for each ROI. The L* variable ranges from 0 to 100 and indicates the lightness or

466 darkness of a color, with higher values indicating lighter shades. The a* variable measures the

467 color's position on the green-to-red axis, where negative values represent green tones and positive

468 values represent red tones. Lastly, the b* variable indicates the color's position on the blue-to-

469 yellow axis, with negative values indicating blue tones and positive values indicating yellow tones

470 [58,60]. To showcase the full capabilities of our portable platform, we also successfully performed

471 the PL colorimetric analysis directly on a smartphone using the MATLAB Mobile app, for both

472 IOs and Android systems (Video S1). As shown in the video, the recorded image is uploaded, the

473 F-CNPs are automatically identified, and the colorimetric evaluations are performed, yielding the

474 average ROI coordinates as final result.

475

476   The results of the colorimetric analyses indicate that a* is affected by high experimental

477   errors, which is consistent with its dependence from the R channel intensity, that in our case only

478   contains noise (Fig. 4c-d). On the other hand, as shown in Fig. S11, L* is found to have the same

479   trend with buffer calibration solution pH, as single-channel fluorescence intensity (e.g. that of B

480   or G channels in Fig. 4e-f, or that of B channel in Fig. S8c). This is consistent with the concept

481   that L* represents the perceptual overall lightness of the observed signal. Thus, this variable could

482   also, in principle, be employed for pH determination through a single-channel fluorescence sensing

483   strategy. However, as delineated in the optimization of pH sensing conditions (see SI, Fig. S8c,

484   Table S3) the single channel methodology typically yields resolutions that do not exceed ±1 pH

485   units. Therefore, a L*-based sensing strategy, akin to a single-channel detection method, was not

486   applied in subsequent analyses of this work.

487   Nonetheless, b* is found to effectively capture the perceptual color transition observed in

488   the pictures with changing pH. This becomes more evident when looking at the perceptual colors

489   given by a variation of b*, when L* and a* are fixed at typical values obtained in the analyzed

490   pictures (color scale legend in Fig. 5c). Specifically, the trend of b* as a function of calibration

491   solution pH can be best fitted using a decreasing exponential function, of the type:

492    $y = a_1 + a_2 \exp(x/a_3)$ (3)

493   yielding $a_1 = 43 \pm 7$, $a_2 = 41 \pm 6$, $a_3 = 9 \pm 3$ and R^2 of 0.99877. From this fitting curve, the 95%

494   confidence interpolation errors result of ±0.2 pH units in the pH range from 2.5 to 6.7 and of ±0.3

495   pH units in the pH range of 6.7 to 7.0.

496   This reveals an improvement compared to typical resolution allowed by the most common

497   commercial pH indicator paper strips [5]. Recent literature works documented paper– or polymer-

498   based colorimetric pH sensing devices that surpass the capabilities of currently available

499   commercial pH paper strips (i.e. ±0.5) [8–11,14–18,21,22] (Table 1). However, it is noteworthy

500   that these studies exhibit certain limitations, including: (i) reliance on costly sensitive materials for

501   pH detection (such as commercially available or custom-synthesized indicator dyes), (ii) complex

502   procedures for substrate patterning (involving methods like laser patterning or customized ink-jet

503   printing), or (iii) a restricted dynamic range spanning only 3–5 pH units [8–22,41,43,61]. In

504   comparison, the sensing method reported herein relies on environmentally sustainable and cost-

505   effective CDs. Moreover, it involves a user-friendly preparation approach and grants rapid pH

506   measurement with uniform resolution across six pH units, requiring very small sample volumes.

507   Table 1: comparison of recently reported portable pH sensing devices based on optical detection.

Sensitive material	Support	Fabrication technique	Signal registration	pH range	pH resolution	Ref.
Thymol blue, methyl red, bromothymol blue, phenolphthalein	Filter paper	Inkjet-printing on filter paper with hydrophilic microfluidic channels	Color scanner (Lab* color space)	5–9	N/A	[18]
Phenol red, chlorophenol red	Whatman Grade 1 filter paper	Drop-casting onto sensing areas of paper microfluidic device	Smartphone (HSV color space)	4–9	±0.17	[21]
Imidazole coumarin dye	Poly(methyl methacrylate)-based polymer network	Dye covalently bound to polymer by copolymerization	Fiber optic device (PL intensity)	10.0–13.2	< 0.5	[17]
Curcumin Nanoparticles (CURNs)	Whatman filter paper no. 1	Drop-casting onto hydrophilic test area of paper	Digital camera (average grayscale intensity)	8–13	±0.15-0.27	[13]
Indicator composed of chlorophenol red, phenol red and phenolphthalein	Whatman filter paper grade 1	Drop-casting on detection areas of paper-based analytical device	Flatbed Scanner (magenta channel intensity)	5–10	±0.2-0.4	[61]
Luminol derivative (LABD)	Functionalized filter paper strips	Filter paper strips immersed in a LABD solution and left to dry	Visual	4.0–11.0	N/A	[10]
Spiropyran derivative	Cellulosic paper	Spiropyran derivative chemically attached to the paper	Visual	1–14	N/A	[19]
Rhodamine derivative (RhA)	Activated cellulose paper	RhA immobilized using a coupling agent	Visual	1–8	N/A	[11]
Two dyes based on anthraquinone and azo chromophores (D-1 and D-2)	Cellulose paper	Screen printing	Spectophotometer (Lab* color space)	6–12 (D1) 1–4 (D2)	N/A	[20]

pH indicators (m-nitrophenol, phenolphthalein, thymolphthalein)	Superomniphobic glass microfiber paper	pH indicators deposited in three domains created by depositing a thin layer of paraffin wax	Visual	7.5–13	N/A	[22]
SISCON pH paper	Whatman Grade 1 filter paper	pH paper attached to filter paper microfluidic channel	Smartphone camera (HSV color space)	3–10	N/A	[15]
8 commercial pH indicators	Mixed cellulose ester (MCE) paper	Inkjet-printing on MCE paper	Color scanner (R, G, B split channel)	1.00–13.60	±0.20	[8]
Polyaniline nanoparticles (PAni-NPs)	Whatman quantitative filter paper (Grade 41)	Filter paper dipped in PAni-NP solution and dried, repeated 7 times	Smartphone camera (R, G, B split channels)	2–10	±0.2 (pH 2-6); ±0.6 (pH 8-10)	[12]
Two BODIPY compounds (1a and 1b)	Whatman filter paper	Paper sheets immersed in BODIPY solutions and air-dried	Visual	0.00–6.59 (1a) 0.00–6.28 (1b)	N/A	[9]
Purposely synthesized quinoxalines	Cellulose filter paper (pore size 8–12 μm)	Paper stips immersed in hot dye solution followed by drying	Visual	1–5	N/A	[16]
CDs from 1,2,4-triaminobenzene and NaOH	pH test strips	CDs incorporated in pH test strips	Visual	1–14	N/A	[41]
CDs from Aphen and citric acid	pH test paper	Inkjet printing	Visual	1–14	N/A	[42]
CDs from terephthalic acid (PTA) and o-phenylenediamine (oPD)	Poly(m-phenylene isophthalamide) (PMIA)	CDs loaded in PMIA from solution followed by casting	Smartphone camera (R, G, B split channels and CIE 1931 color space)	1–14	±0.2	[43]
Resorcinol-derived CDs	Nitrocellulose-based platform	Drop-casting of pristine CDs solution on nitrocellulose pads	Smartphone camera (PL analysis in Lab* color space)	2.2–7	±0.2 (pH 2.5-6.7) ±0.3 (pH 6.7-7.0)	This work

508 Furthermore, the present work highlights the integration of colorimetric analysis on fluorescence

509 data acquired by portable devices to enable highly accurate sensing measurements. In fact, this is

510 evidenced by the significantly lower resolution obtained applying a single-channel fluorescence

511 detection (see SI, Table S3). Similar colorimetric analysis of fluorescence data obtained by

512 portable devices was previously reported only in very few previous reports [62,63]. In this work,

513 the fluorescence analysis approach leads to significant advance of the sensing accuracy, thanks to

514 its capability of harnessing simultaneously the sensing information coming from the blue and the

515 green PL bands of the CDs. Overall, given the resolution and dynamic range attainable with this

516   method, it appears as an effective combination of accuracy and practical operational efficacy.

517   Therefore, the presented portable pH sensing platform is particular suited for practical applications

518   where existing compact pH meters fail to meet necessary requirements of robustness or

519   integrability within critical operational conditions. Similar problems could be pervasive of

520   disparate areas, including biological samples, food chemical analyses, water quality assessment,

521   and others [4,64–66].

522   **4. Conclusions**

523   In summary, a pH sensing platform based on nitrocellulose was developed based on the

524   employment of CDs containing acid/base responsive PPs. First, through a comprehensive analysis

525   of the fluorescence response of the CDs upon incremental addition of small amounts of HCl and

526   NaOH, we established correlations between observed spectroscopic changes and the acid-base

527   protonation-deprotonation equilibria of PPs within the CDs. This approach also enabled to devise

528   a titration-based method, estimating an order of magnitude range for the concentration of CDs in

529   solution. Subsequently, the CDs were used to functionalize CNPs in the nitrocellulose platform.

530   After suitable calibrations, namely, of CD concentration, pH of pristine CD dispersion, image

531   acquisition conditions and application of a fluorescence colorimetry image analysis (evaluating

532   CIELAB b* coordinate), we demonstrated the achievement of a high resolution for pH reaching

533   ±0.2 pH units in the pH range 2.5 – 6.7 and of ±0.3 pH units in the pH range: 6.7 – 7.0.

534   pH sensing with the resolution and dynamic range here shown could be profitable for a

535   very broad range of applicative areas, including food, water, and biological sample analysis. In

536   particular, this portable platform offers a solution to the challenges posed by delicate and expert-

537   personnel requiring potentiometric pH-meters.

538   Looking ahead, enhancing the sensing capabilities of these platforms could be achieved

539   through advancements in platform design and optical detection systems, as well as by optimizing

the surface chemistry of CDs, tailored for specific sample types. Such developments could pave the way for broader adoption of safe and cost-effective nanoparticles like CDs in fluorescent nitrocellulose-based portable pH sensing technologies.

Acknowledgements

References

[1]   R.P. Buck, S. Rondinini, A.K. Covington, F.G.K. Baucke, C.M.A. Brett, M.F. Camoes,
       M.J.T. Milton, T. Mussini, R. Naumann, K.W. Pratt, P. Spitzer, G.S. Wilson, Measurement
       of pH. Definition, standards, and procedures (IUPAC Recommendations 2002), Pure Appl.
       Chem. 74 (2002) 2169–2200. https://doi.org/10.1351/pac200274112169.

[2]   H.J. Park, J.H. Yoon, K.G. Lee, B.G. Choi, Potentiometric performance of flexible pH
       sensor based on polyaniline nanofiber arrays, Nano Converg. 6 (2019) 9.
       https://doi.org/10.1186/s40580-019-0179-0.

[3]   P. Spitzer, K.W. Pratt, The history and development of a rigorous metrological basis for pH
       measurements, J. Solid State Electrochem. 15 (2011) 69–76.
       https://doi.org/10.1007/s10008-010-1106-9.

[4]   W. Xiao, Q. Dong, The Recent Advances in Bulk and Microfluidic-Based pH Sensing and
       Its Applications, Catalysts 12 (2022) 1124. https://doi.org/10.3390/catal12101124.

[5]   J. Guo, L. Qiu, Z. Deng, F. Yan, Plastic reusable pH indicator strips: preparation via anion-
       exchange of poly(ionic liquids) with anionic dyes, Polym. Chem. 4 (2013) 1309–1312.
       https://doi.org/10.1039/C2PY21076B.

[6]   G. Li, H. Su, N. Ma, G. Zheng, U. Kuhn, M. Li, T. Klimach, U. Pöschl, Y. Cheng,
       Multifactor colorimetric analysis on pH-indicator papers: an optimized approach for direct
       determination of ambient aerosol pH, Atmospheric Meas. Tech. 13 (2020) 6053–6065.
       https://doi.org/10.5194/amt-13-6053-2020.

[7]   A. Collins, R.B. Scott, C.R. Hirsch, C. Ottaviani, C. Krahé, F. Meeten, A systematic review
       of the literature on interpretation bias and its physiological correlates, Biol. Psychol. 173
       (2022).

[8]   Y. Li, Y. Wang, S. Chen, Z. Wang, L. Feng, Inkjet-printed paper-based sensor array for
       highly accurate pH sensing, Anal. Chim. Acta 1154 (2021) 338275.

[9]   D. Öztürk, İ. Ömeroğlu, B. Köksoy, C. Göl, M. Durmuş, A BODIPY decorated multiple
       mode reusable paper-based colorimetric and fluorometric pH sensor, Dyes Pigments 205
       (2022) 110510. https://doi.org/10.1016/j.dyepig.2022.110510.

[10]   Z. Yan, X. Zhang, C. Bao, H. Tang, Q. Zhao, L. Hu, J. You, A novel luminol derivative and
       its functionalized filter-paper for reversible double-wavelength colorimetric pH detection in
       fruit juice, Sens. Actuators B Chem. 262 (2018) 869–875.
       https://doi.org/10.1016/j.snb.2018.02.100.

[11]   T. Taweetanavanich, B. Wanno, T. Tuntulani, B. Pulpoka, C. Kaewtong, A pH optical and
       fluorescent sensor based on rhodamine modified on activated cellulose paper, J. Chin.
       Chem. Soc. 66 (2019) 493–499. https://doi.org/10.1002/jccs.201800327.

[12]   T. Lee, H.-T. Lee, J. Hong, S. Roh, D. Yeon Cheong, K. Lee, Y. Choi, Y. Hong, H.-J.
       Hwang, G. Lee, A regression-based machine learning approach for pH and glucose
       detection with redox-sensitive colorimetric paper sensors, Anal. Methods 14 (2022) 4749–
       4755. https://doi.org/10.1039/D2AY01329K.

[13]   N. Pourreza, H. Golmohammadi, Application of curcumin nanoparticles in a lab-on-paper
       device as a simple and green pH probe, Talanta 131 (2015) 136–141.
       https://doi.org/10.1016/j.talanta.2014.07.063.

[14]   J. Ling, G. Naren, J. Kelly, T.S. Moody, A.P. de Silva, Building pH Sensors into Paper-
       Based Small-Molecular Logic Systems for Very Simple Detection of Edges of Objects, J.
       Am. Chem. Soc. 137 (2015) 3763–3766. https://doi.org/10.1021/jacs.5b00665.

[15] O.R. Chanu, A. Kapoor, V. Karthik, Digital image analysis for microfluidic paper based pH sensor platform, Mater. Today Proc. 40 (2021) S64–S68. https://doi.org/10.1016/j.matpr.2020.03.503.

[16] E.V. Ermakova, A.V. Bol'shakova, A. Bessmertnykh-Lemeune, Dual-Responsive and Reusable Optical Sensors Based on 2,3-Diaminoquinoxalines for Acidity Measurements in Low-pH Aqueous Solutions, Sensors 23 (2023) 2978. https://doi.org/10.3390/s23062978.

[17] T.H. Nguyen, T. Venugopala, S. Chen, T. Sun, K.T.V. Grattan, S.E. Taylor, P.A.M. Basheer, A.E. Long, Fluorescence based fibre optic pH sensor for the pH 10–13 range suitable for corrosion monitoring in concrete structures, Sens. Actuators B Chem. 191 (2014) 498–507. https://doi.org/10.1016/j.snb.2013.09.072.

[18] K. Abe, K. Suzuki, D. Citterio, Inkjet-Printed Microfluidic Multianalyte Chemical Sensing Paper, Anal. Chem. 80 (2008) 6928–6934. https://doi.org/10.1021/ac800604v.

[19] A. Abdollahi, A. Mouraki, M.H. Sharifian, A.R. Mahdavian, Photochromic properties of stimuli-responsive cellulosic papers modified by spiropyran-acrylic copolymer in reusable pH-sensors, Carbohydr. Polym. 200 (2018) 583–594. https://doi.org/10.1016/j.carbpol.2018.08.042.

[20] H. Zhang, A. Hou, K. Xie, A. Gao, Smart color-changing paper packaging sensors with pH sensitive chromophores based on azo-anthraquinone reactive dyes, Sens. Actuators B Chem. 286 (2019) 362–369. https://doi.org/10.1016/j.snb.2019.01.165.

[21] N. Lopez-Ruiz, V.F. Curto, M.M. Erenas, F. Benito-Lopez, D. Diamond, A.J. Palma, L.F. Capitan-Vallvey, Smartphone-Based Simultaneous pH and Nitrite Colorimetric Determination for Paper Microfluidic Devices, Anal. Chem. 86 (2014) 9554–9562. https://doi.org/10.1021/ac5019205.

[22] S. Movafaghi, M.D. Cackovic, W. Wang, H. Vahabi, A. Pendurthi, C.S. Henry, A.K. Kota, Superomniphobic Papers for On-Paper pH Sensors, Adv. Mater. Interfaces 6 (2019) 1900232. https://doi.org/10.1002/admi.201900232.

[23] H. LEE, M.R. HAM, H. KIM, S. KIM, Hydrogel coating composition for chemical sensor and chemical sensor fabricated using same, WO2022030754A1, 2022.

[24] Y.S. KIM, Y.-B. CHO, T.-S. JUN, C.K. KIM, Paper ph sensor using colorimetric method and preparation method thereof, WO2016159488A1, 2016.

[25] K. Perez, L. NELSON, T. Robinson, A. FREANEY, H. VAN, A. OLANREWAJU, G.C. VALENTINE, E.J. Seibel, E. Fan, J.D. POSNER, M. SHARMA, Sensor paper and methods for use, WO2023086993A1, 2023.

[26] H. Ehtesabi, Z. Hallaji, S. Najafi Nobar, Z. Bagheri, Carbon dots with pH-responsive fluorescence: a review on synthesis and cell biological applications, Microchim. Acta 187 (2020) 150. https://doi.org/10.1007/s00604-019-4091-4.

[27] V.M. Naik, S.V. Bhosale, G.B. Kolekar, A brief review on the synthesis, characterisation and analytical applications of nitrogen doped carbon dots, Anal. Methods 14 (2022) 877–891. https://doi.org/10.1039/D1AY02105B.

[28] A.O. Adeola, A. Clermont-Paquette, A. Piekny, R. Naccache, Advances in the design and use of carbon dots for analytical and biomedical applications, Nanotechnology 35 (2023) 012001. https://doi.org/10.1088/1361-6528/acfdaf.

[29] S. Chahal, J.-R. Macairan, N. Yousefi, N. Tufenkji, R. Naccache, Green synthesis of carbon dots and their applications, RSC Adv. 11 (2021) 25354–25363. https://doi.org/10.1039/D1RA04718C.

651   [30] J. Wan, X. Zhang, Y. Jiang, S. Xu, J. Li, M. Yu, K. Zhang, Z. Su, Regulation of multi-color
652   fluorescence of carbonized polymer dots by multiple contributions of effective conjugate
653   size, surface state, and molecular fluorescence, J. Mater. Chem. B 10 (2022) 6991–7002.
654   https://doi.org/10.1039/D2TB01330D.
655   [31] B. Han, X. Hu, X. Zhang, X. Huang, M. An, X. Chen, D. Zhao, J. Li, The fluorescence
656   mechanism of carbon dots based on the separation and identification of small molecular
657   fluorophores, RSC Adv. 12 (2022) 11640–11648. https://doi.org/10.1039/D2RA00431C.
658   [32] A. Sharma, J. Das, Small molecules derived carbon dots: synthesis and applications in
659   sensing, catalysis, imaging, and biomedicine, J. Nanobiotechnology 17 (2019) 92.
660   https://doi.org/10.1186/s12951-019-0525-8.
661   [33] A. Sharma, T. Gadly, S. Neogy, S.K. Ghosh, M. Kumbhakar, Molecular Origin and Self-
662   Assembly of Fluorescent Carbon Nanodots in Polar Solvents, J. Phys. Chem. Lett. 8 (2017)
663   1044–1052. https://doi.org/10.1021/acs.jpclett.7b00170.
664   [34] S. Qu, H. Chen, X. Zheng, J. Cao, X. Liu, Ratiometric fluorescent nanosensor based on
665   water soluble carbon nanodots with multiple sensing capacities, Nanoscale 5 (2013) 5514–
666   5518. https://doi.org/10.1039/C3NR00619K.
667   [35] Q. Zhao, Y. Li, W. Wei, J. Huang, D. Lu, S. Liu, X. Shi, A ratiometric fluorescence-based
668   colorimetric sensor for the portable analysis of antioxidants via smartphone, Microchem. J.
669   190 (2023) 108625. https://doi.org/10.1016/j.microc.2023.108625.
670   [36] H. Nie, M. Li, Q. Li, S. Liang, Y. Tan, L. Sheng, W. Shi, S.X.-A. Zhang, Carbon Dots with
671   Continuously Tunable Full-Color Emission and Their Application in Ratiometric pH
672   Sensing, Chem. Mater. 26 (2014) 3104–3112. https://doi.org/10.1021/cm5003669.
673   [37] J. Zhang, H. Chen, K. Xu, D. Deng, Q. Zhang, L. Luo, Current Progress of Ratiometric
674   Fluorescence Sensors Based on Carbon Dots in Foodborne Contaminant Detection,
675   Biosensors 13 (2023) 233. https://doi.org/10.3390/bios13020233.
676   [38] W.K. Szapoczka, C. Olla, C. Carucci, A.L. Truskewycz, T. Skodvin, A. Salis, C.M.
677   Carbonaro, B. Holst, P.J. Thomas, Ratiometric Fluorescent pH Sensing with Carbon Dots:
678   Fluorescence Mapping across pH Levels for Potential Underwater Applications,
679   Nanomaterials 14 (2024) 1434. https://doi.org/10.3390/nano14171434.
680   [39] A. Heering, M. Lahe, M. Vilbaste, J. Saame, J. Paulo Samin, I. Leito, Improved pH
681   measurement of mobile phases in reversed-phase liquid chromatography, Analyst (2024).
682   https://doi.org/10.1039/D3AN02029K.
683   [40] L. Deleebeeck, A. Snedden, D. Nagy, Z. Szilágyi Nagyné, M. Roziková, M. Vičarová, A.
684   Heering, F. Bastkowski, I. Leito, R. Quendera, V. Cabral, D. Stoica, Unified pH
685   Measurements of Ethanol, Methanol, and Acetonitrile, and Their Mixtures with Water,
686   Sensors 21 (2021) 3935. https://doi.org/10.3390/s21113935.
687   [41] L. Wang, M. Li, W. Li, Y. Han, Y. Liu, Z. Li, B. Zhang, D. Pan, Rationally Designed
688   Efficient Dual-Mode Colorimetric/Fluorescence Sensor Based on Carbon Dots for
689   Detection of pH and Cu2+ Ions, ACS Sustain. Chem. Eng. 6 (2018) 12668–12674.
690   https://doi.org/10.1021/acssuschemeng.8b01625.
691   [42] T. Zhang, S. Dong, F. Zhao, M. Deng, Y. Fu, C. Lü, Tricolor emissive carbon dots for
692   ultra-wide range pH test papers and bioimaging, Sens. Actuators B Chem. 298 (2019)
693   126869. https://doi.org/10.1016/j.snb.2019.126869.
694   [43] K. Huo, J. Zhang, T. Lin, Y. Zhang, Y. Liu, X. Liu, Colorimetric and fluorescent dual-
695   mode pH sensor with PMIA as substrate and CQDs as probe for high accuracy detection of

696   full range pH, Dyes Pigments 219 (2023) 111574.
697   https://doi.org/10.1016/j.dyepig.2023.111574.
698 [44] G. Minervini, A. Panniello, A. Madonia, C.M. Carbonaro, F. Mocci, T. Sibillano, C.
699   Giannini, R. Comparelli, C. Ingrosso, N. Depalo, E. Fanizza, M.L. Curri, M. Striccoli,
700   Photostable carbon dots with intense green emission in an open reactor synthesis, Carbon
701   198 (2022) 230–243. https://doi.org/10.1016/j.carbon.2022.07.034.
702 [45] T.C. McIlvaine, A BUFFER SOLUTION FOR COLORIMETRIC COMPARISON, J. Biol.
703   Chem. 49 (1921) 183–186. https://doi.org/10.1016/S0021-9258(18)86000-8.
704 [46] G. Knobel, On The Capillary Electrophoresis Of Monohydroxy Metabolites Of Polycyclic
705   Aromatic Hydrocarbons And Its Application To The Analysis Of Biological Matrices,
706   Electron. Theses Diss. (2013). https://stars.library.ucf.edu/etd/2858.
707 [47] H. Rastogi, S. Jana, Evaluation of physicochemical properties and intestinal permeability of
708   six dietary polyphenols in human intestinal colon adenocarcinoma Caco-2 cells, Eur. J.
709   Drug Metab. Pharmacokinet. 41 (2016) 33–43. https://doi.org/10.1007/s13318-014-0234-5.
710 [48] T. Mao, F.N.U. Akshit, I. Matiwalage, S. Sasidharan, C.M. Alvarez, P. Wescombe, M.S.
711   Mohan, Preferential Binding of Polyphenols in Blackcurrant Extracts with Milk Proteins
712   and the Effects on the Bioaccessibility and Antioxidant Activity of Polyphenols, Foods 13
713   (2024) 515. https://doi.org/10.3390/foods13040515.
714 [49] J. Shang, X. Gao, Nanoparticle counting: towards accurate determination of the molar
715   concentration, Chem Soc Rev 43 (2014) 7267–7278. https://doi.org/10.1039/C4CS00128A.
716 [50] W. Bae, T.-Y. Yoon, C. Jeong, Direct evaluation of self-quenching behavior of
717   fluorophores at high concentrations using an evanescent field, PLOS ONE 16 (2021)
718   e0247326. https://doi.org/10.1371/journal.pone.0247326.
719 [51] J. Wachlmayr, C. Hannesschlaeger, A. Speletz, T. Barta, A. Eckerstorfer, C. Siligan, A.
720   Horner, Scattering versus fluorescence self-quenching: more than a question of faith for the
721   quantification of water flux in large unilamellar vesicles?, Nanoscale Adv. 4 (2022) 58–76.
722   https://doi.org/10.1039/D1NA00577D.
723 [52] W.F. Watson, R. Livingston, Self-Quenching and Sensitization of Fluorescence of
724   Chlorophyll Solutions, J. Chem. Phys. 18 (2004) 802–809.
725   https://doi.org/10.1063/1.1747779.
726 [53] Y. Song, S. Zhu, S. Xiang, X. Zhao, J. Zhang, H. Zhang, Y. Fu, B. Yang, Investigation into
727   the fluorescence quenching behaviors and applications of carbon dots, Nanoscale 6 (2014)
728   4676–4682. https://doi.org/10.1039/C4NR00029C.
729 [54] J. Wang, Y. Yang, X. Liu, Solid-state fluorescent carbon dots: quenching resistance
730   strategies, high quantum efficiency control, multicolor tuning, and applications, Mater.
731   Adv. 1 (2020) 3122–3142. https://doi.org/10.1039/D0MA00632G.
732 [55] F. Zu, F. Yan, Z. Bai, J. Xu, Y. Wang, Y. Huang, X. Zhou, The quenching of the
733   fluorescence of carbon dots: A review on mechanisms and applications, Microchim. Acta
734   184 (2017) 1899–1914. https://doi.org/10.1007/s00604-017-2318-9.
735 [56] C. Wei, S. Hu, F. Liang, Z. Song, X. Liu, One-pot synthesis of concentration and excitation
736   dual-dependency truly full-color photoluminescence carbon dots, Chin. Chem. Lett. 33
737   (2022) 4116–4120. https://doi.org/10.1016/j.cclet.2022.01.053.
738 [57] C.J. Reckmeier, J. Schneider, Y. Xiong, J. Häusler, P. Kasák, W. Schnick, A.L. Rogach,
739   Aggregated Molecular Fluorophores in the Ammonothermal Synthesis of Carbon Dots,
740   Chem. Mater. 29 (2017) 10352–10361. https://doi.org/10.1021/acs.chemmater.7b03344.

741 [58] J. Schanda, International Commission on Illumination, eds., Colorimetry: understanding the
742   CIE system, CIE/Commission internationale de l'eclairage ; Wiley-Interscience, [Vienna,
743   Austria] : Hoboken, N.J, 2007.
744 [59] J. Schanda, CIE u′, v′ Uniform Chromaticity Scale Diagram and CIELUV Color Space, in:
745   M.R. Luo (Ed.), Encycl. Color Sci. Technol., Springer, New York, NY, 2016: pp. 185–188.
746   https://doi.org/10.1007/978-1-4419-8071-7_12.
747 [60] C. Oleari, Standard colorimetry: definitions, algorithms, and software, John Wiley & Sons,
748   Inc, Chichester, West Sussex, UK, 2016.
749 [61] J. Noiphung, M.P. Nguyen, C. Punyadeera, Y. Wan, W. Laiwattanapaisal, C.S. Henry,
750   Development of Paper-Based Analytical Devices for Minimizing the Viscosity Effect in
751   Human Saliva, Theranostics 8 (2018) 3797–3807. https://doi.org/10.7150/thno.24941.
752 [62] J. Yang, Z. Li, Q. Jia, Design of dual-emission fluorescence sensor based on Cu
753   nanoclusters with solvent-dependent effects: Visual detection of water via a smartphone,
754   Sens. Actuators B Chem. 297 (2019) 126807. https://doi.org/10.1016/j.snb.2019.126807.
755 [63] Spatially confining copper nanoclusters in porous ZrO2 for
756   fluorescence/colorimetry/smartphone triple-mode detection of metoprolol tartrate, Biosens.
757   Bioelectron. 231 (2023) 115290. https://doi.org/10.1016/j.bios.2023.115290.
758 [64] L. Manjakkal, S. Dervin, R. Dahiya, Flexible potentiometric pH sensors for wearable
759   systems, RSC Adv. 10 (2020) 8594–8617. https://doi.org/10.1039/D0RA00016G.
760 [65] M.T. Ghoneim, A. Nguyen, N. Dereje, J. Huang, G.C. Moore, P.J. Murzynowski, C.
761   Dagdeviren, Recent Progress in Electrochemical pH-Sensing Materials and Configurations
762   for Biomedical Applications, Chem. Rev. (2019).
763   https://doi.org/10.1021/acs.chemrev.8b00655.
764 [66] Y. Tang, L. Zhong, W. Wang, Y. He, T. Han, L. Xu, X. Mo, Z. Liu, Y. Ma, Y. Bao, S. Gan,
765   L. Niu, Recent Advances in Wearable Potentiometric pH Sensors, Membranes 12 (2022)
766   504. https://doi.org/10.3390/membranes12050504.
767